

## On Tropical Cyclone Footprints in Sea Surface Height Anomalies

P. D. Pivaev<sup>1,2</sup>✉, V. N. Kudryavtsev<sup>1,2</sup>

<sup>1</sup> *Marine Hydrophysical Institute of RAS, Sevastopol, Russian Federation*

<sup>2</sup> *Russian State Hydrometeorological University, Saint Petersburg, Russian Federation*

✉ [pivaev.pavel@gmail.com](mailto:pivaev.pavel@gmail.com)

### Abstract

*Purpose.* Tropical cyclones leave ‘footprints’ on the ocean surface in the form of sea surface height anomalies, which are well observed by satellite altimeters. Recent studies have shown that the values of these anomalies, normalized by the square of the maximum wind speed in the tropical cyclone and the acceleration due to gravity, are a universal function of a dimensionless parameter composed of the radius of maximum wind speed, translation speed of the tropical cyclone and the buoyancy frequency in the seasonal pycnocline. The purpose of this paper is to investigate physical processes responsible for the formation of tropical cyclone wakes in sea surface height anomalies, assess contribution of barotropic and baroclinic modes, and substantiate and quantify the self-similarity of hurricane-induced sea surface height anomalies revealed in satellite altimetry.

*Methods and Results.* The paper considers sea surface height anomalies in wakes of tropical cyclones observed in different regions of the World Ocean from 2010 to 2020. The modelling is carried out using a simplified model of the baroclinic and barotropic response of the ocean to moving tropical cyclones. Calculations show that the first and second baroclinic modes make a significant contribution to the sea surface height anomaly, and the contribution of the third baroclinic mode is of secondary importance. The relative contribution of the barotropic mode depends substantially on the local ocean depth, and it is greater when the ocean is shallower. However, the contribution of the barotropic mode to satellite altimetry measurements of the ocean surface height in wakes of tropical cyclones can be ignored, since the lifetime of the barotropic perturbation is significantly shorter than a typical time interval between the passage of the tropical cyclone and the measurements.

*Conclusions.* Empirical parameterizations of satellite altimetry measurements of the sea surface height anomaly in wakes of tropical cyclones can be reproduced by superposition of the first three baroclinic modes describing the ocean response to the tropical cyclone passage. In this case, the best fit of the modelling results to the measurement data is achieved if the ocean surface drag coefficient at hurricane-force winds has an approximately constant value of  $2.25 \cdot 10^{-3}$ . This result can be considered as an estimate of the momentum exchange between the ocean and the atmosphere at hurricane-force winds, which remains a subject of present-day scientific effort.

**Keywords:** tropical cyclone, sea surface height, satellite altimeter, sea surface height anomaly, baroclinic mode, barotropic mode, sea surface height parameterization

**Acknowledgements:** This work was supported by the Ministry of Science and Education of the Russian Federation under state assignments No. FNNN-2024-0001 (Marine Hydrophysical Institute of RAS) and No. FSZU-2025-0005 (Russian State Hydrometeorological University).

**For citation:** Pivaev, P.D. and Kudryavtsev, V.N., 2025. On Tropical Cyclone Footprints in Sea Surface Height Anomalies. *Physical Oceanography*, 32(3), pp. 408-426.

© 2025, P. D. Pivaev, V. N. Kudryavtsev

© 2025, Physical Oceanography



## Introduction

Tropical cyclones (TCs) propagating over the ocean result in barotropic and baroclinic disturbances. These disturbances manifest themselves as perturbations of the sea surface height (SSH). The author of [1] was the first to study the impact of the barotropic mode on the ocean surface. Using a two-layer fluid approximation as an example, the author showed that the steady-state displacement of the free surface produced by a point source of vorticity moving in a straight line has the form of a trough along its trajectory. The depth of the trough exponentially decays in the cross-track direction, with the decay rate being the inverse of the barotropic radius of deformation. He also obtained a solution for baroclinic displacements of the interface between the two layers, but the author did not consider the manifestation of these displacements in variations of the SSH. The authors of [2] gave analytical expressions for the SSH anomaly associated with the barotropic mode and the currents corresponding to this mode. The authors derived relations that are applicable to wind fields resembling those of real atmospheric cyclones. Using numerical modelling, the authors also obtained SSH anomalies associated with the baroclinic mode and showed that in the case of a two-layer fluid, baroclinic SSH anomalies are out of phase with and proportional to the displacements of the interface between the two layers (pycnocline) with a proportionality coefficient equal to the relative difference in densities of the two layers.

With the advent of satellite altimetry data, it became possible to experimentally study SSH anomalies produced by moving TCs. At present, surface height anomalies can be considered well documented. The results of [3–5] show that SSH anomalies observed by altimeters are described quite well by the relationship

$$\frac{h_s g}{U_m^2} = c_s \frac{N_1 R_m}{V}, \quad (1)$$

where  $g$  – acceleration due to gravity;  $h_s$  – SSH anomaly;  $U_m$  – maximum wind speed in the TC;  $N_1$  – buoyancy frequency in the seasonal thermocline;  $R_m$  – radius of maximum wind speed in the TC;  $V$  – TC translation speed, and  $c_s$  – empirical constant. Experimental estimates of the proportionality constant in the equation (1) from the works mentioned are  $c_s = 6.9 \cdot 10^{-6}$  [3, 4] and  $c_s = 8.6 \cdot 10^{-6}$  [5].

Expression (1) was obtained in [3] using the condition of pressure continuity across the ocean surface and the pycnocline displacements in a two-layer model, taken from [1], considered as a scale of TC-induced displacements in continuously stratified ocean. Accordingly, equation (1) was initially obtained for the first baroclinic mode, whereas SSH anomalies analyzed in [4, 5] have, as a matter of fact, an unknown mode composition.

In processing altimetry data, the authors of [4, 5] excluded cases with a local ocean depth of less than 2 and 5 km, respectively. The authors assumed that using this depth-based filtration of data allowed them to minimize the contribution of the barotropic mode to the displacement of the ocean surface, and the approximation of SSH anomalies by equation (1) then becomes justified. The assumption that the exclusion of barotropic surface displacements is possible by simply discarding the data according to the ocean depth criterion requires clarification. Indeed, according to [1], the ratio of the barotropic displacement of the ocean surface to

the displacement of the interface in a two-layer fluid is equal to the ratio of the corresponding radii of deformation:

$$\frac{h_{bt}}{\eta_{bc}} = \frac{R_{bc}}{R_{bt}} = \left( \frac{\varepsilon H_1}{H} \right)^{1/2},$$

where  $H_1$  – upper layer thickness;  $H$  – ocean depth;  $\varepsilon$  – relative density difference. As shown in [2], the displacement of the ocean surface associated with the baroclinic mode is well described by the formula  $h_{bc} = \varepsilon \eta_{bc}$ , which means that the ratio of the barotropic SSH anomaly to the baroclinic one is

$$\frac{h_{bt}}{h_{bc}} = \left( \frac{H_1}{\varepsilon H} \right).$$

When substituting values typical for the ocean  $\varepsilon = 10^{-3}$ ,  $H_1 = 200$  m,  $H = 5000$  m, we obtain a ratio of the order of unity, which means that barotropic and baroclinic displacements of the ocean surface are comparable even in conditions of a sufficiently deep ocean. For this reason, the influence of the barotropic mode on SSH anomalies parameterized by formula (1) remains unclear. In addition, the role of higher-order baroclinic modes in the formation of the SSH anomaly is also unclear. If their role is significant, it is necessary to explain why SSH anomalies observed experimentally in [3–5] are well parameterized by the law (1), which assumes the dominant role of the first baroclinic mode.

The aim of our study is to analyze SSH anomalies produced by moving TCs and their parameterization taking into account the barotropic response and the multimode structure of the baroclinic response of the ocean to the passage of the TC.

## Model and input parameters

### Main equations

To model the SSH anomaly, we use a simplified model of the baroclinic and barotropic response of the ocean to a moving TC proposed in [6]. The model equations are written for the unbounded, inviscid fluid consisting of three layers – seasonal, main pycnocline and abyssal. In each layer, buoyancy frequencies are constant (zero in the abyssal). The model is based on the linearized equations of motion in Boussinesq approximations on an  $f$ -plane, written in a coordinate system whose origin is fixed at the TC centre. The initial condition is a horizontally homogeneous ocean at rest. The stationary solution of the problem in coordinate system moving with TC is considered. The driving force is the ‘frozen’ wind stress field of the TC moving along the  $x$ -axis (in opposite direction) with a constant speed  $V$ . The details of constructing the wind vector field in the TC are given in the next section. Equations for the barotropic mode are obtained assuming the ocean with uniform density.

Under the approximations mentioned above, the displacement of the ocean surface relative to the undisturbed state (SSH anomaly) is determined as

$$h(x, y) = \frac{1}{V} \int_{-\infty}^x w(x', y, 0) dx', \quad (2)$$

where  $w(x, y, 0)$  is the vertical velocity at the surface associated with either baroclinic or barotropic modes.

The barotropic vertical velocity is given by the Fourier integral:

$$w_{bt}(x, y) = \frac{-f}{C_{bt}^2} \frac{1}{(2\pi)^2} \iint_{-\infty}^{+\infty} dk dl P(k, l) e^{-i(kx+ly)}. \quad (3)$$

The function  $P(k, l)$  is defined as

$$P(k, l) = \frac{\hat{F}(k, l)}{(1 - (V/C_{bt})^2)k^2 + l^2 + \alpha_{bt}^2}$$

and  $\hat{F}(k, l)$  is the two-dimensional Fourier transform of the curl of the wind stress  $\tau(x, y)$  in TC:

$$\begin{aligned} \hat{F}(k, l) &= \iint_{-\infty}^{+\infty} dx dy F(x, y) e^{i(kx+ly)}, \\ F(x, y) &= \frac{(\nabla \cdot \tau)_z}{\rho_0}. \end{aligned}$$

In the equations above,  $k, l$  – components of the wave vector;  $f$  – Coriolis parameter;  $C_{bt} = \sqrt{gH}$  – phase speed of long waves ( $g$  – acceleration due to gravity,  $H$  – ocean depth) and  $\alpha_{bt} = f/C_{bt}$  – reciprocal of the barotropic radius of deformation.

The vertical velocity at the surface, associated with the  $n$ -th baroclinic mode, is found using the dynamic boundary condition at the sea surface, according to which the velocity at the level  $z = 0$  is proportional to the vertical gradient of the vertical velocity at the surface:

$$w_{bc}^{(n)}(x, y, 0) = \left(\frac{C_n^2}{g}\right) \frac{\partial w_{bc}^{(n)}(x, y, 0)}{\partial z}, \quad (4)$$

where  $C_n$  – eigenvalue (long wave speed) for the  $n$ -th baroclinic mode (see Appendix for the calculation of eigenvalues). Three-dimensional field of vertical velocity of the  $n$ -th baroclinic mode is represented as the product of two functions:

$$w_{bc}^{(n)}(x, y, z) = W_z^{(n)}(z) W_{xy}^{(n)}(x, y).$$

The function  $W_z^{(n)}(z)$ , depending on the vertical coordinate, has the following piecewise-smooth form in the three-layer ocean approximation:

$$W_z^{(n)}(z) = \begin{cases} a_{1n} \sin(N_1 z/C_n), & z > -d_1, \\ a_{2n} \sin(N_2[z + d_2]/C_n + \phi_n), & -d_2 < z < -d_1, \\ a_{2n}(z + H)/(H - d_2) \sin \phi_n, & z < -d_2, \end{cases}$$

where  $d_1, d_2$  – depths of lower boundaries of seasonal and main pycnoclines, respectively,  $N_1, N_2$  – buoyancy frequencies corresponding to the two layers. Original equations for nondimensional coefficients  $a_{1n}$  и  $a_{2n}$  are given in [6, p. 3483]. In this study, we modified them to allow for a more accurate description of the finite-depth effects that can influence the shape of  $W_z^{(n)}(z)$ . The modified expressions for  $a_{1n}$  and  $a_{2n}$  as well as expressions for  $\phi_n$  are given in Appendix at the end the article.

Taking into account the above expressions for the baroclinic vertical velocity, the dynamic boundary condition (4) can be rewritten as

$$w_{bc}^{(n)}(x, y, 0) = g^{-1} a_{1n} N_1 C_n W_{xy}^{(n)}(x, y). \quad (5)$$

The function  $W_{xy}^{(n)}(x, y)$ , depending on the horizontal coordinates, is given by two different Fourier integrals. The choice of the integral depends on the ratio between the TC translation speed  $V$  and the long wave speed for the  $n$ -th baroclinic mode. At  $V > C_n$ , the function  $W_{xy}^{(n)}(x, y)$  is determined by one-dimensional integrals:

$$W_{xy}^{(n)}(x, y) = \frac{f}{(V^2 - C_n^2)} \frac{1}{2\pi} \int_{-\infty}^{\infty} dl k_n^{-1} Q_n(x, l) e^{-ily},$$

$$Q_n(x, l) = \int_{-\infty}^x dx' \hat{F}(x, l) \sin k_n(x - x'),$$

where

$$\hat{F}(x, l) = \int_{-\infty}^{\infty} dy F(x, y) e^{ily}$$

is the one-dimensional Fourier transform of the wind stress curl in the TC, and

$$k_n = \sqrt{\frac{l^2 + \alpha_n^2}{(V/C_n)^2 - 1}},$$

where  $\alpha_n = f/C_n$  – reciprocal of the  $n$ -th baroclinic radius of deformation.

At  $V < C_n$ , the baroclinic vertical velocity has a spatial shape similar to that of the barotropic velocity:

$$W_{xy}^{(n)}(x, y) = \frac{f}{C_n^2} \frac{1}{(2\pi)^2} \iint_{-\infty}^{+\infty} dk dl P_n(k, l) e^{-i(kx+ly)},$$

where

$$P_n(k, l) = \frac{\hat{F}(k, l)}{(1 - (V/C_n)^2)k^2 + l^2 + \alpha_n^2}.$$

Thus, by applying equation (2) to equations (3) and (5), one can obtain two-dimensional fields of the SSH anomaly associated with the barotropic and baroclinic modes excited by the moving TC.

As can be seen from equation (3) and the function  $W_{xy}^{(n)}(x, y)$  in equation (5), the forcing exciting the vertical motion in the ocean according to the model [6] is represented by the wind stress curl only. Terms associated with the wind stress divergence and atmospheric pressure perturbation, which could be, in general, included in equation (3) and the expression for  $W_{xy}^{(n)}(x, y)$  in equation (5), are not considered in [6]. This is due to the fact that it is the wind stress vorticity that determines the steady-state response of the ocean to the TC passage in the form of SSH anomaly measured by altimeters. As shown in [1, 7–9], significant disturbances of the SSH caused by atmospheric pressure anomaly in the TC and wind stress divergence are localized in the area under the TC eye and disappear in its wake, i.e., after the TC passage. Since the probability of an altimeter taking measurements in the vicinity of the TC eye is rather small (in [4, 5] the time delay between the TC passage and the altimeter measurement ranged from 0 to 7 days), the contribution of

atmospheric pressure anomalies and wind stress divergence in the TC to the SSH anomaly measured by satellite altimeters can be easily assumed to be virtually zero.

Further, we will show that the barotropic SSH anomaly obtained with equations (3) and (2) has a shape of a trough, extended along the TC trajectory and decaying in the cross-track direction, with the decay rate being the inverse of the barotropic radius of deformation [1]. The baroclinic SSH anomaly field obtained with equations (5) and (2) under the condition  $V < C_n$  has a shape of a trough as well, which, however, decays at the rate equal to the inverse of the baroclinic radius of deformation. If the TC translation velocity  $V > C_n$ , then the trough is superimposed by a wave wake resulting from the excitation of inertia-gravity waves. The kinematic properties of this wake were analyzed in detail in [1].

We expect that satellite altimetry data reflects SSH anomalies formed by the superposition of barotropic and baroclinic displacements of the ocean surface behind TCs, which are discussed in the next section.

### TC and stratification parameters

In this section, we apply the model described above to model SSH anomalies produced by real TCs. We consider TCs that existed in different regions of the World Ocean from 2010 to 2020. We selected those TCs whose category did not fall below category one on the Saffir-Simpson scale for at least one day. The total number of TCs satisfying this condition was 417. Data on the location of TCs, their maximum wind speed  $U_m$  and translation speed  $V$  were taken from the IBTrACS database [10] (variables with the *usa\_* prefix), in which the time series have 3-hour time resolution.

To construct a two-dimensional wind field, we use the model of tangential wind speed in the TC proposed in [11]. To apply this model, we used information on the radii of reference wind speeds (34, 50 and 60 kt) in different quadrants of TCs, which is available in the IBTrACS. The resulting profile of the tangential wind speed is set equal to the profile of the wind vector magnitude. To specify a two-dimensional wind vector field, we introduced an inflow angle of  $22.5^\circ$ , which is a measure of the deviation of the wind direction from purely cyclonic one. The radius of the maximum wind speed  $R_m$ , which is necessary for subsequent analysis, was determined as the radius at which the wind speed profile obtained with [11] attains its maximum. For the analysis, we retained TC positions at which the condition  $U_m/(fR_m) \geq 10$  was satisfied, because the model [11] reproduces the maximum wind speed in the TC only in the limit  $U_m/(fR_m) \ll 1$ . An example of the wind speed radial profile is shown in Fig. 1, *a*.

It follows from the previous section that one of the input parameters of the model is the wind stress curl at the surface of the ocean. The wind stress vector was calculated using the standard relationship:

$$\boldsymbol{\tau} = \rho_a C_d |\mathbf{U}| \mathbf{U},$$

where  $\rho_a = 1.15 \text{ kg}\cdot\text{m}^{-3}$  – air density;  $\mathbf{U}$  – wind vector, and  $C_d$  – sea surface drag coefficient calculated in the same way as in [12]. At  $U_m < 40 \text{ m}\cdot\text{s}^{-1}$   $C_d$  behaves like the drag coefficient in equation (18) [3], where we used  $C_d$  from COARE3.5 [13] as a reference. At  $U_m > 40 \text{ m}\cdot\text{s}^{-1}$   $C_d$  equals 0.0015. The wind-speed dependence of  $C_d$  is shown in Fig. 1, *b*. An example of wind stress curl radial profile is shown in Fig. 1, *c*.

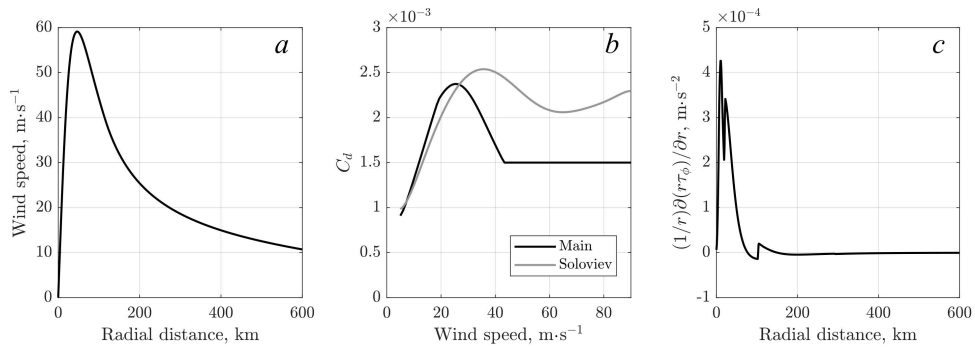


**Fig. 1.** Radial profile of wind speed obtained using the model [11] (a); dependence of the drag coefficient on the wind speed (the black line is  $C_d$  from [12] used throughout this study; the gray line is the drag coefficient from [14] (b); radial profile of wind stress curl (the variable on the vertical axis divided by sea water density) (c)

To define the ocean stratification, we use temperature and salinity profiles from the MAXSS Storm Atlas <sup>1</sup> (product – atlas of multi-source earth observations over tropical cyclones for the time period 2010–2020). The four-dimensional datasets (three spatial dimensions and one time dimension) are Argo float data interpolated onto a regular spatiotemporal grid (ISAS20 product <sup>2</sup>). The temperature and salinity data have monthly time resolution, a spatial resolution of  $0.5^\circ$  in longitude, and a variable resolution in latitude. The vertical grid with 187 grid points covers the water column from the surface to 5500 m depth. The temperature and salinity profiles at the TC positions were obtained using the linear interpolation in space and time. The potential density of seawater was calculated from these profiles using the TEOS10 thermodynamic equation of state <sup>3</sup>. Finally, the potential density profiles were converted to those of the buoyancy frequency (see Figs. 2, a, b). We note that the three-layer approximation of the water column in the model [6] performs poorly when the local ocean depth is low. Therefore, we excluded those TC positions which had local depths less than 200 m from consideration.

The model of the baroclinic and barotropic ocean response [6] was derived for idealized conditions in which the TC parameters are constant in time, the ocean stratification is horizontally uniform, and the changes in the Coriolis parameter with latitude are not taken into account. To apply this model to real conditions, we assume that the parameters  $U_m$ ,  $R_m$ , and  $V$  corresponding to a given TC at a given time are constant, and the buoyancy frequency profile obtained from the temperature and salinity profiles interpolated onto the TC location point is horizontally uniform.

<sup>1</sup> Piollé, J.-F., Reul, N. and De Boyer-Montégut, C., 2023. *Atlas of Multi-Source Earth Observations over Tropical Cyclone (2010-2020) for ESA MAXSS Project*. Ver. 1.0. Plouzane, France: Ifremer. [Accessed: 07.12.2022]. <https://doi.org/10.12770/6C56BCDE-050F-42EB-92B8-8E882E1F4DB9>

<sup>2</sup> Kolodziejczyk, N., Prigent-Mazella, A. and Gaillard, F., 2023. *ISAS Temperature, Salinity, Dissolved Oxygen Gridded Fields*. SEANOE. <https://doi.org/10.17882/52367>

<sup>3</sup> McDougall, T.J. and Barker, P.M., 2011. *Getting Started with TEOS-10 and the Gibbs Seawater (GSW) Oceanographic Toolbox: Version 3.0*. CSIRO Marine and Atmospheric Research, 28 p.

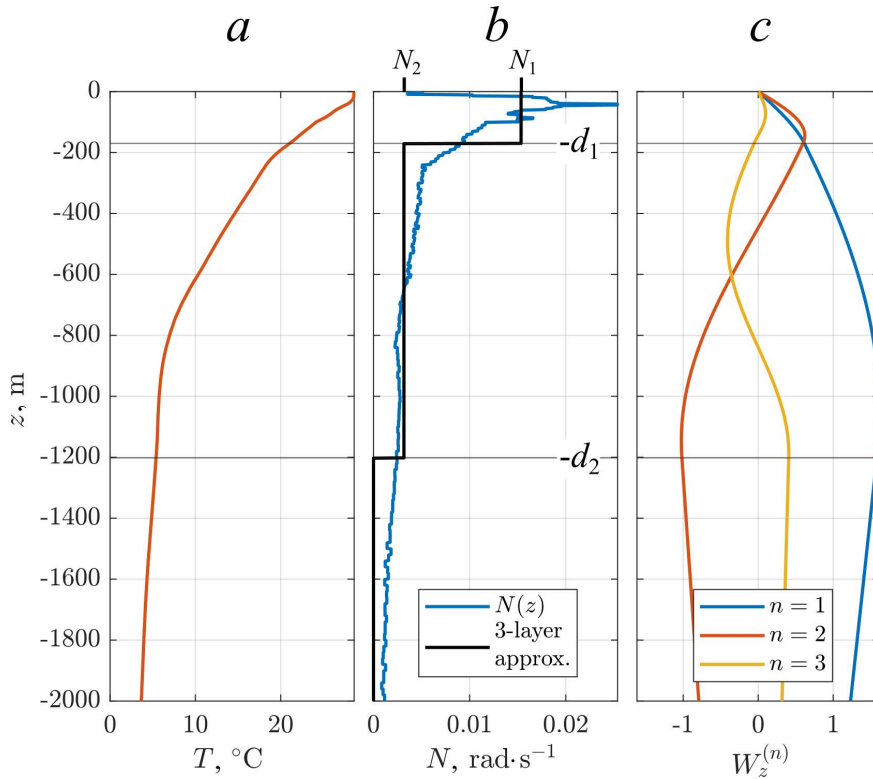


**Fig. 2.** Initial temperature profile (a), initial buoyancy frequency profile (b), and profiles of the first three baroclinic modes of vertical velocity (c). The result of breaking the water column into three layers based on the buoyancy frequency profile is shown in the center figure, where the horizontal lines denote the lower boundaries of the seasonal and main pycnocline, respectively, and the black line shows the piecewise constant buoyancy frequency profile used in the model. To display the details of the vertical distribution of the parameters near the ocean surface, the depth range is limited to 2 km. The ocean depth in this case is 4.8 km

Then, the model is run in the idealized computational domain, in which two-dimensional fields of the SSH anomaly associated with the baroclinic and barotropic modes and their superposition are calculated. The computational domain in the horizontal plane has the shape of a square with a side of  $2R_{bt}$ , where  $R_{bt}$  is the barotropic radius of deformation at the given TC position, and the spatial resolution is set to  $R_m/5$ .

The total number of TCs left in our database after the removal of TC positions based on local depth and values of  $U_m/(fR_m)$  parameter was 400.

## Results

### Examples of modelled baroclinic and barotropic TC-induced SSH anomalies

To illustrate the modelled SSH anomaly described in the previous section, we consider a specific example of TC Igor – category 4 TC that occurred in the North Atlantic in 2010. At 15:00 UTC on 15 September 2010, the TC had the following parameters: maximum wind speed  $U_m = 59.1 \text{ m}\cdot\text{s}^{-1}$ , translation speed  $V = 3.2 \text{ m}\cdot\text{s}^{-1}$ , coordinates of the TC eye  $19.6^\circ\text{N}$ ,  $55.0^\circ\text{W}$ . The radial profile of the wind speed in

the TC, constructed using the model [11], is shown in Fig. 1, *a*, and the corresponding profile of the wind stress curl is shown in Fig. 1, *c*. According to the wind model, the radius of the maximum wind speed  $R_m$  was 41.9 km. The temperature and salinity profiles obtained by spatiotemporal interpolation of ISAS20 data onto the given TC position are shown in Fig. 2. The same figure shows the buoyancy frequency profile and vertical velocity eigenfunctions for the first three baroclinic modes.

SSH anomalies of the first three baroclinic modes calculated using equations (2) and (5) are shown in Fig. 3, *a*, *b* and *c*. The baroclinic response possesses wave oscillations associated with inertia-gravity waves characteristic of these conditions, in which  $C_n$  do not exceed the TC translation speed. The wave-filled wake has features typical of a baroclinic response: higher-order modes have a longer wavelength and a smaller wedge angle. In addition to wave motions on the ocean surface, the baroclinic response also consists of a trough (see Fig. 5, *a*). The amplitude of wave oscillations and the magnitude of the surface trough weaken as the mode number increases. The shape of the sea surface corresponding to the barotropic mode calculated using equations (2) and (3), has no wave-filled wake, but a trough aligned with the TC track (Figs. 3, *d*, 4, *d* and 5, *a*).

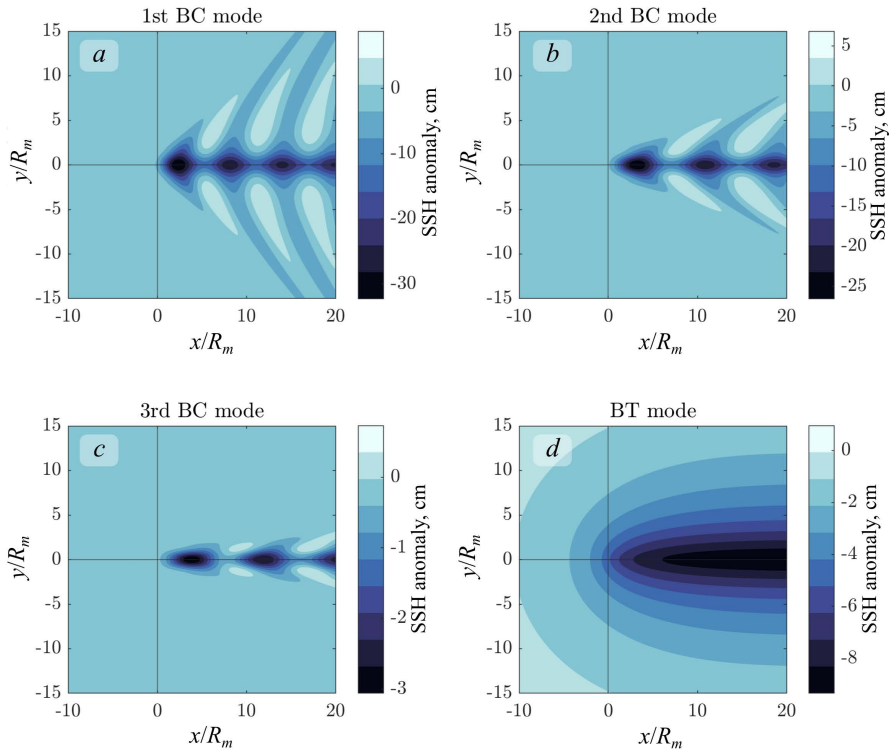


**Fig. 3.** SSH anomaly in the deep ocean (4.8 km depth), corresponding to the first baroclinic mode (*a*), second mode (*b*), third mode (*c*), and barotropic mode (*d*). Parameters  $x/R_m$  and  $y/R_m$  represent the distance from the TC eye normalized by the radius of maximum wind speed. TC parameters in this particular case are  $U_m = 59.1 \text{ m}\cdot\text{s}^{-1}$ ,  $R_m = 41.9 \text{ km}$ ,  $V = 3.2 \text{ m}\cdot\text{s}^{-1}$ , latitude =  $19.6^\circ$

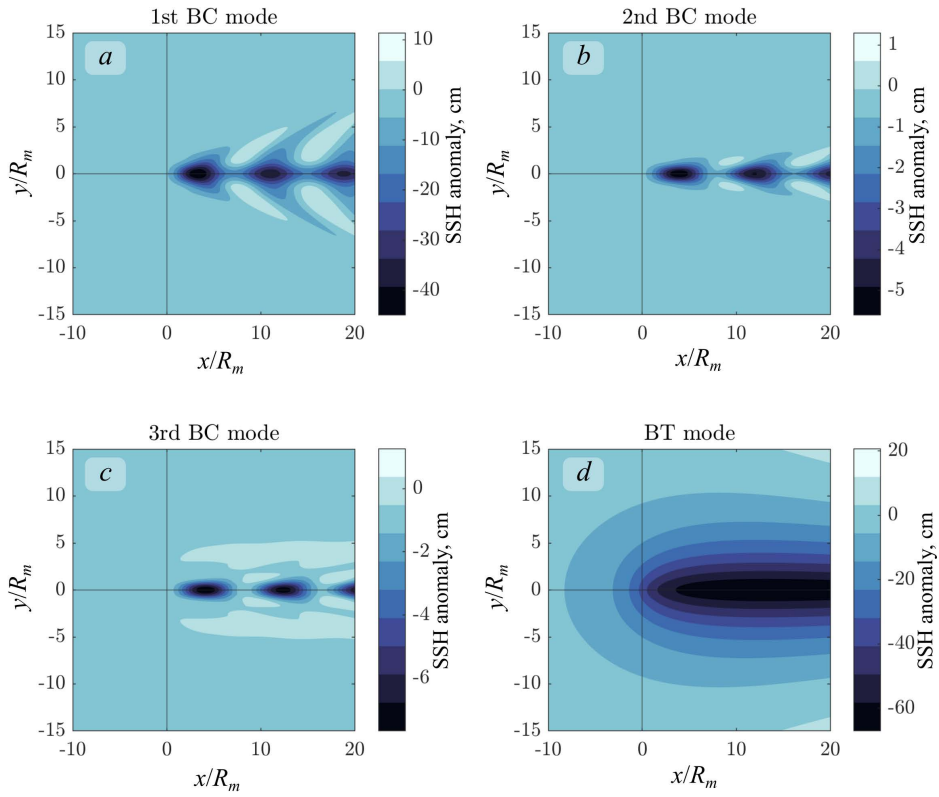


**Fig. 4.** The same as in Fig. 3 but in the shallow ocean (0.5 km depth)

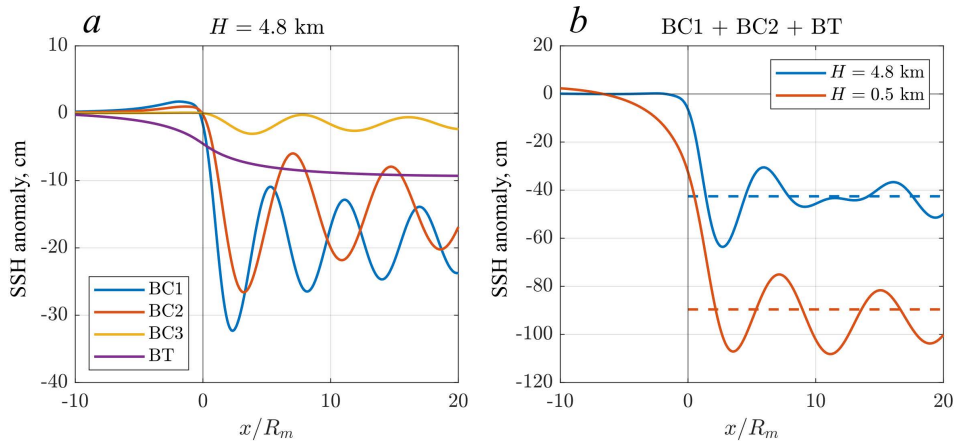


**Fig. 5.** Transections of the two-dimensional SSH anomaly fields along the line  $y/R_m = 0$ , corresponding to the first (BC1), second (BC2), third (BC3) baroclinic modes and the barotropic mode (BT) from Fig. 3 (a), corresponding to the superposition of the first two baroclinic modes and the barotropic mode in deep (blue line) and shallow (orange line) ocean conditions (b). The dashed horizontal lines show the average SSH anomaly, which is analyzed and used in comparison with SSH anomalies calculated from the parameterizations [3–5]

If we decrease the ocean depth, the long wave speeds  $C_n$  for the baroclinic modes decrease, which leads to changes in the shape of the wave-filled wake: the wavelength becomes greater and the wedge angle becomes smaller, as shown in Fig. 4 (cf. Fig. 3). At the same time, the decrease in the ocean depth leads to a significant increase in the barotropic displacement of the sea surface (cf. Fig. 4,  $d$  with Fig. 3,  $d$ ). We will address the dependence of the barotropic SSH anomaly on the local ocean depth in the next section.

To compare the modelled SSH anomalies with the observed ones described by the relation (1), we use the average SSH anomaly along the line  $y/R_m = 0$  at  $x/R_m > 0$ . The choice of the average anomaly is justified by the fact that the altimeter acquisition time has a random shift relative to the time of TC passage through a given point in the sea surface (in studies [4, 5] this shift reached 7 days). Therefore, when considering a large dataset of satellite altimeter measurements, SSH anomalies induced by inertia-gravity waves give a zero contribution, and it is the average TC-induced surface displacement (displacement left after the TC passage), associated with troughs of baroclinic and barotropic modes, that dominates the altimetry signal.

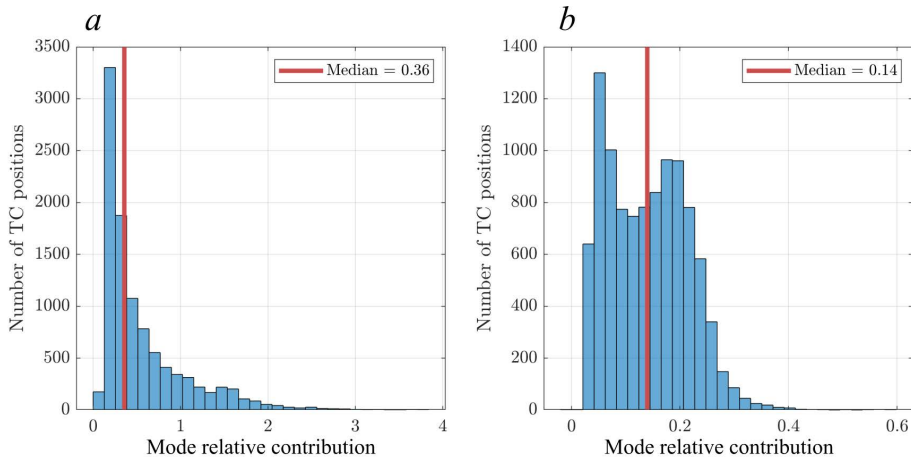
### **Modelling of TC-induced SSH anomalies in the World Ocean**

In the same way the model was applied to TC Igor in the previous section, we applied the model to simulate and then calculate SSH anomalies produced by all the TCs from the considered set at different points of the World Ocean at different times. At each TC position, we calculated the average SSH anomaly produced by different modes and their superposition (as in Fig. 5). These calculations are analyzed here.

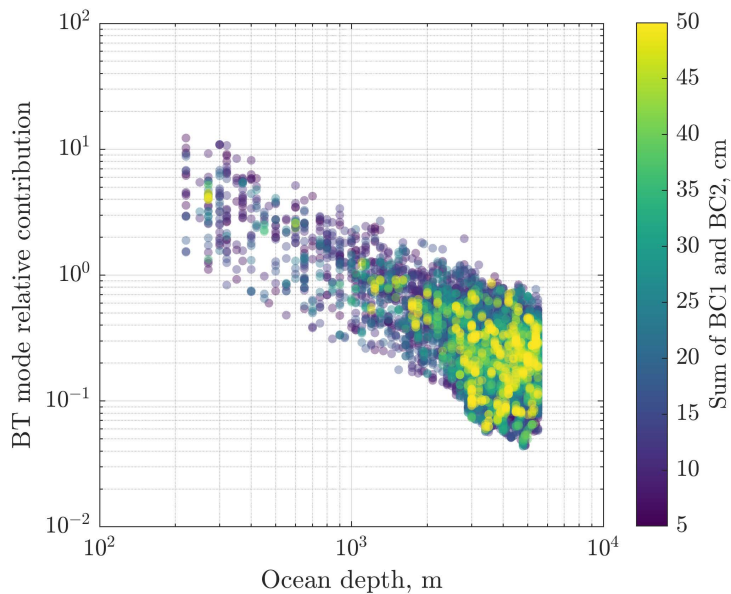
Fig. 6 shows the relative contribution of the second and third baroclinic modes to the SSH anomaly. The contribution of the second baroclinic mode to the modelled SSH is significant. In 50% of cases, the second baroclinic mode leads to an increase in the average SSH anomaly by more than 36%. Among these, we can also highlight cases in which taking into account the second mode leads to an increase in the average SSH anomaly by a factor 2 or greater. The contribution of the third mode to the baroclinic SSH anomalies leads to a less significant effect. In the overwhelming majority of cases, accounting for the third mode leads to SSH anomaly increase that does not exceed 30%, and in half of the cases the increase in the anomaly does not exceed 14% compared to the average SSH anomaly produced by the superposition of the first two baroclinic modes.

Fig. 7 shows the relative contribution of the barotropic mode to the average SSH anomaly produced by the superposition of first two baroclinic modes and the barotropic mode. It follows that even at the ocean depth of 5.5 km, barotropic mode accounts for 20% of the total SSH anomaly caused by the two baroclinic modes and the barotropic mode, which means that the barotropic mode cannot be considered negligible. At depths less than 2 km, barotropic SSH anomalies can be more significant, and at depths less than 500 m, taking into account the barotropic motions, can increase the total SSH anomaly by more than a factor of two. The color coding in Fig. 7 shows that the barotropic mode increases the SSH anomaly associated with the two baroclinic modes by more than 100% in situations when the total baroclinic SSH does not exceed 50 cm. Note that in Fig. 7 the maximum depth is 5.5 km, which is the maximum depth in the ISAS20 database. If, however,

we consider ocean depths taken, for example, from the ETOPO database, the results in cases where the ocean depth exceeds 5.5 km remain practically unchanged.



**Fig. 6.** Histogram showing the contribution of the second baroclinic mode to the average SSH anomaly calculated from the first baroclinic mode (*a*), the contribution of the baroclinic third mode to the average SSH anomaly calculated from the superposition of the first and second baroclinic modes (*b*). Red vertical lines show median values



**Fig. 7.** Contribution of the barotropic mode to the average SSH anomaly produced by the first two baroclinic modes as a function of the local ocean depth

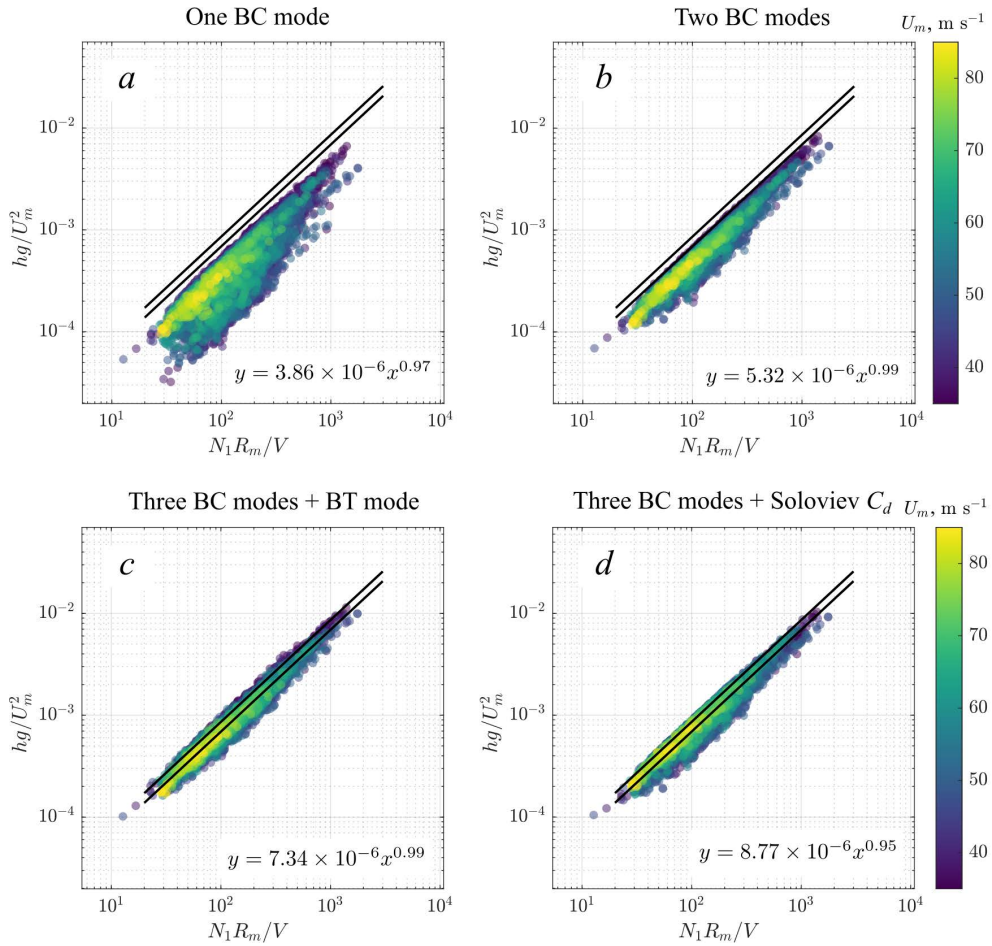


**Fig. 8.** Average SSH anomaly normalized by  $U_m^2/g$  as a function of the parameter  $N_1 R_m / V$ , calculated from the first baroclinic mode (a), the superposition of the first two baroclinic modes (b), and the superposition of the first three baroclinic modes and the barotropic mode (c), obtained from the superposition of the first three baroclinic modes modelled using the drag coefficient from [14] (d). Black lines show the parameterizations from [3, 4] (lower black line), and from [5] (upper black line). Only the cases in which the local ocean depth was greater than 2 km are shown

Fig. 8, a shows the modelling results in dimensionless variables dictated by equation (1). To be consistent with [4, 5], we excluded cases with the local depths less than 2 km from Fig. 8. It is evident that SSH anomalies calculated from only the first baroclinic mode follow the power-like law, but the ‘level’ of the modelled anomalies significantly underestimates that of the parameterizations obtained in [3–5]. Indeed, the proportionality coefficient of the power law fit to the modelled SSH anomaly in dimensionless variables is  $3.85 \times 10^{-6}$  as opposed to  $6.9 \cdot 10^{-6}$  from [3, 4]. If we add the second baroclinic mode to the first mode, the power-law dependence becomes more pronounced, and the level of the modelled SSH anomaly increases significantly (Fig. 8, b). Despite these improvements, the average SSH anomaly still does not reach the level of anomalies predicted by the parameterizations of [3–5]. Addition of the third baroclinic mode and

the barotropic mode separately to the superposition of the first two baroclinic modes does not significantly improve the results. If, however, we add both of these modes, the SSH anomalies represented by the superposition of three baroclinic modes and the barotropic mode are appreciably enhanced, leading to significant improvement in the agreement between the modelled and parameterized SSH anomalies (Fig. 8, *c*).

Approximation of the modelling results by the relation (1) shows that the exponent, equal to 0.99, practically coincides with unity, and the proportionality constant, equal to  $7.46 \cdot 10^{-6}$ , is between the values of the constants in the parameterizations [3, 4] ( $6.9 \cdot 10^{-6}$ ) and [5] ( $8.6 \cdot 10^{-6}$ ). This result indicates that TC-induced SSH anomalies measured by altimeters are composed of not only several baroclinic modes but apparently the barotropic mode even in deep ocean conditions with depths exceeding 2 km.

### Discussion

Fig. 8, *c* shows that the observed SSH anomalies produced by moving TCs, presented in the form (1), are reproduced by the superposition of the first three baroclinic modes and the barotropic mode. However, in the model [6], the changes in the Coriolis parameter with latitude were not taken into account. As noted in [1], the currents corresponding to the barotropic trough and the baroclinic ridge (lifted pycnocline) should respond to the changes in the Coriolis parameter with latitude. It means that the steady-state barotropic and baroclinic perturbations should be altered by breakdown into planetary waves. The time required for the breakdown is given in [15] and is estimated as one day for the barotropic trough and several weeks for the baroclinic ridge. We conclude that the barotropic component happens to be substantially dissolved by planetary wave radiation by the time the altimeter passes over the TC track, since the time lag between the altimeter acquisition time and TC passage time is likely to be greater than one day. Based on this, consideration of the barotropic component when interpreting satellite altimeter measurements seems unjustified.

In this context, we consider the modelled SSH anomalies in Fig. 8, *c* as unrealistic. Unfortunately, as we noted in the previous section, the superposition of three baroclinic modes, producing a more stable perturbation of SSH, underestimates observed SSH anomalies presented in the form of parameterizations [3–5] (Fig. 9). To improve the agreement between the model and parameterizations [3–5], we consider wind-dependence of the drag coefficient different from that used so far (Fig. 1, *c*).

Little is known about the behavior of the drag coefficient at wind speeds greater than  $40\text{--}50 \text{ m}\cdot\text{s}^{-1}$ . Experimental estimates differ from one another even in terms of tendencies. For example, the results of studies [16, 17] indicate an almost constant value of the drag coefficient at hurricane winds, which ranges from 0.002 to 0.0025. In turn, the results of recent studies [3, 18, 19, 5] suggest a decrease in the drag coefficient with increasing wind speed. The authors of [14] proposed a different parameterization of the resistance law based on the results of laboratory experiments and numerical modelling. In that study, there is no monotonic attenuation of the drag coefficient with increasing wind speed. At wind speeds greater than  $25 \text{ m}\cdot\text{s}^{-1}$ , this parameterization gives systematically larger values of  $C_d$  (around  $2.25 \cdot 10^{-3}$ ) compared to that used in our calculations so far (see Fig. 1, *b*).

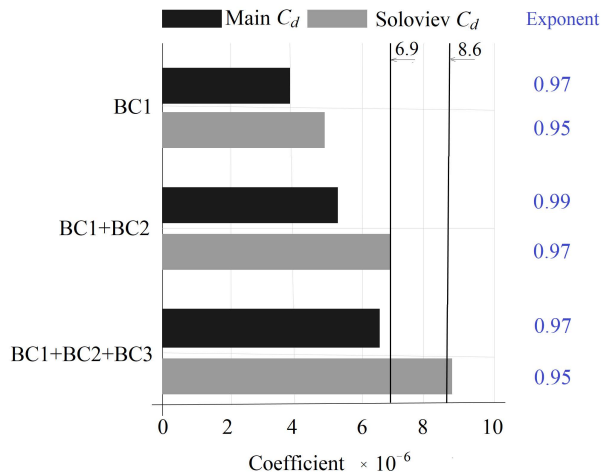


**Fig. 9.** Values of proportionality constants in the approximation of modelled SSH anomalies by a power function of the form (1) for different combinations of modes and using different drag coefficients. Black and gray bars correspond to calculations with the drag coefficients shown by black and gray lines in Fig. 1, *b* respectively. Numbers in blue show the exponents in the approximation of modelled SSH anomalies by a power function (1). Horizontal lines show the values of the proportionality coefficients in the parameterizations [3, 4] –  $6.9 \cdot 10^{-6}$  and [5] –  $8.6 \cdot 10^{-6}$

If we apply the parameterization [14] to estimate the wind stress and repeat the calculation SSH anomalies associated with the superposition of the first three baroclinic modes, the agreement between the modelled surface displacements and the displacements predicted by the parameterizations [3–5] is noticeably improved (Fig. 8, *d*). The approximation of the modelled SSH anomalies by the power function (1) has the proportionality constant  $8.77 \cdot 10^{-6}$  which is close to  $8.6 \cdot 10^{-6}$  – the proportionality constant in the parameterization [5]. Fig. 9 shows how the results change in terms of the proportionality constant and the exponent in the approximation of the modelled SSH anomalies by expression (1) when considering different combinations of baroclinic modes. It is evident that usage of  $C_d$  from [12], whatever the combination of baroclinic modes, cannot reproduce parameterizations [3–5]. On the other hand, usage of  $C_d$  from [14] results in better agreement with the mentioned parameterizations when two or three baroclinic modes are considered. If a more definite choice of the mode combination is needed then the superposition of three baroclinic modes is the optimal one. This is because low-wind-speed points cluster slightly below the power law approximation of the modelled SSH anomalies, and they are uniformly distributed between the parameterizations [3–5]. The better performance of the drag coefficient from [14] in modelling SSH anomalies is in some contradiction with the conclusions of work [3], in which it was shown that  $C_d$  for hurricane-force winds should decay with increasing wind speed, ensuring asymptotically constant wind stresses at extremely high wind speeds (see Fig. 15 in [3]).

## Conclusion

In this paper, we analyzed the formation of TC footprints in sea surface height (SSH) anomalies that are observed by satellite altimeters, and which have simple parameterization in the form of relation (1) [3–5]. For the analysis, a simplified model of the barotropic and baroclinic response of the ocean to moving TCs proposed in [6] was used. The model was applied to simulate SSH anomalies produced by TCs of the first category and higher, which propagated in different regions of the World Ocean in the time period from 2010 to 2020. SSH anomalies were simulated for 400 TCs using observed TC parameters and ocean stratification.

The main factor determining the steady-state SSH anomaly in the wake of the TC is the vorticity of the wind stress. The atmospheric pressure anomaly in the TC and the divergence of the wind stress generates significant disturbances of the sea surface directly under the TC, which, however, fade out in the wake and therefore do not significantly contribute to the steady-state SSH anomaly which dominates satellite altimeter signal.

Applying the model [6] to the global set of TCs, we showed that the relative contribution of the second baroclinic mode to the SSH anomaly compared to the first mode is significant and is more than 36% in half of the modelled cases. The contribution of the third baroclinic mode relative to the superposition of the first two is not as significant and does not exceed 30% with a median value of 14%.

Addition of the barotropic mode to the superposition of the first two baroclinic modes results in an increase in the ocean surface displacement. In the ocean with a local depth exceeding 2 km, the influence of the barotropic mode is appreciable so that this mode can increase SSH anomaly associated with the first two baroclinic modes by about 100%. With decreasing depth, addition of the barotropic mode can increase the total SSH anomaly (barotropic plus two baroclinic) by more than 100%. However, the geostrophic currents associated with the barotropic perturbation of the sea surface is less stable than the baroclinic one, so that the barotropic trough is altered by the radiation of planetary waves on time scales of the order of one day [1, 15]. Therefore, it can be expected that the barotropic surface displacements are absent in the altimetry data on the SSH anomalies parameterized in [3–5], because in these studies the time delay between local altimeter measurements and TC passage reached 7 days.

Analysis of modelled TC-induced SSH anomalies in dimensionless variables clearly indicated that the ocean surface displacements which were parameterized in [3–5] are multimodal. The average level of the observed SSH anomalies is well reproduced by the superposition of three baroclinic modes when the drag coefficient proposed in [14] is used to calculate the wind stress. This conclusion differs from the results of the study [3], from which it follows that in the range of hurricane-force winds the drag coefficient decreases monotonically with increasing wind speed.

## Appendix

Dimensionless coefficients in the equation for  $W_z^{(n)}(z)$  are given by the following expressions:

$$a_{1n} = -\left(\frac{2}{\Sigma_n}\right) \frac{\cos(\Sigma_n + \phi_n) - r \cos(\delta_n - \phi_n)}{\cos(\Sigma_n + \phi_n)(1 + \Phi_{\Sigma n}) - r(\delta_n/\Sigma_n)\cos(\delta_n - \phi_n)(1 - \Phi_{\delta n})}$$

$$a_{2n} = -\left(\frac{2}{\Sigma_n}\right) \frac{2N_1/(N_1 - N_2)}{\cos(\Sigma_n + \phi_n)(1 + \Phi_{\Sigma n}) - r(\delta_n/\Sigma_n)\cos(\delta_n - \phi_n)(1 - \Phi_{\delta n})},$$

where

$$\Phi_{\Sigma n} = \frac{\partial \phi_n}{\partial \Sigma_n} = \frac{C_n \sin^2(\phi_n)}{N_2(H - d_2)\Sigma_n}$$

$$\Phi_{\delta n} = \frac{\partial \phi_n}{\partial \delta_n} = \frac{C_n \sin^2(\phi_n)}{N_2(H - d_2)\delta_n}$$

and  $r = (N_1 - N_2)/(N_1 + N_2)$ . Variables  $\Sigma_n = \Sigma(C_n)$ ,  $\delta_n = \delta(C_n)$ ,  $\phi_n = \phi(C_n)$  are defined by the following functions evaluated at  $C = C_n$ :

$$\Sigma(C) = \frac{N_1 d_1}{c} + \frac{N_2(d_2 - d_1)}{c},$$

$$\delta(C) = \frac{N_1 d_1}{c} - \frac{N_2(d_2 - d_1)}{c},$$

$$\phi(C) = \arcsin \frac{N_2(H - d_2)/C}{\sqrt{1 + [N_2(H - d_2)/C]^2}}.$$

Separation constants  $C_n$  are calculated as roots of the transcendental equation (values of  $C_n$  decrease with the mode number  $n$ ):

$$\sin(\Sigma(C) + \phi(C)) - r \sin(\delta(C) - \phi(C)) = 0.$$

## REFERENCES

1. Geisler, J.E., 1970. Linear Theory of the Response of a Two Layer Ocean to a Moving Hurricane. *Geophysical Fluid Dynamics*, 1(1-2), pp. 249-272. <http://doi.org/10.1080/03091927009365774>
2. Ginis, I. and Sutyrin, G., 1995. Hurricane-Generated Depth-Averaged Currents and Sea Surface Elevation. *Journal of Physical Oceanography*, 25(6), pp. 1218-1242. [https://doi.org/10.1175/1520-0485\(1995\)025<1218:HGDACA>2.0.CO;2](https://doi.org/10.1175/1520-0485(1995)025<1218:HGDACA>2.0.CO;2)
3. Kudryavtsev, V., Monzikova, A., Combot, C., Chapron, B., Reul, N. and Quilfen, Y., 2019. A Simplified Model for the Baroclinic and Barotropic Ocean Response to Moving Tropical Cyclones: 1. Satellite Observations. *Journal of Geophysical Research: Oceans*, 124(5), pp. 3446-3461. <http://doi.org/10.1029/2018JC014746>
4. Combot, C., Mouche, A., De Boyer Montegut, C. and Chapron, B., 2024. Toward Comprehensive Understanding of Air-Sea Interactions under Tropical Cyclones: On the Importance of High Resolution and Multi-Modal Observations. *Geophysical Research Letters*, 51(19), e2024GL110637. <http://doi.org/10.1029/2024GL110637>
5. Zhang, B., Wen, L., Perrie, W. and Kudryavtsev, V., 2024. Sea Surface Height Response to Tropical Cyclone from Satellite Altimeter Observations and SAR Estimates. *IEEE Transactions on Geoscience and Remote Sensing*, 62, pp. 1-9. <http://doi.org/10.1109/tgrs.2024.3371168>

6. Kudryavtsev, V., Monzikova, A., Combot, C., Chapron, B. and Reul, N., 2019. A Simplified Model for the Baroclinic and Barotropic Ocean Response to Moving Tropical Cyclones: 2. Model and Simulations. *Journal of Geophysical Research: Oceans*, 124(5), pp. 3462-3485. <http://doi.org/10.1029/2018JC014747>
7. Orlanski, I. and Polinsky, L.J., 1983. Ocean Response to Mesoscale Atmospheric Forcing. *Tellus A: Dynamic Meteorology and Oceanography*, 35, pp. 296-323.
8. Price, J.F., 1983. Internal Wave Wake of a Moving Storm. Part I. Scales, Energy Budget and Observations. *Journal of Physical Oceanography*, 13(6), pp. 949-965. [http://doi.org/10.1175/1520-0485\(1983\)013<0949:IWVOAM>2.0.CO;2](http://doi.org/10.1175/1520-0485(1983)013<0949:IWVOAM>2.0.CO;2)
9. Khain, A. and Sutyurin, G., 1983. *Tropical Cyclones and Their Interaction with the Ocean*. Leningrad: Hydrometeoizdat, 272 p. (in Russian).
10. Knapp, K.R., Kruk, M.C., Levinson, D.H., Diamond, H.J. and Neumann, C.J., 2010. The International Best Track Archive for Climate Stewardship (IBTrACS): Unifying Tropical Cyclone Data. *Bulletin of the American Meteorological Society*, 91(3), pp. 363-376. <http://doi.org/10.1175/2009BAMS2755.1>
11. Chavas, D.R., Lin, N. and Emanuel, K.A., 2015. A Model for the Complete Radial Structure of the Tropical Cyclone Wind Field. Part I: Comparison with Observed Structure. *Journal of the Atmospheric Sciences*, 72(9), pp. 3647-3662.
12. Kudryavtsev, V.N. and Pivaev, P.D., 2025. Mixed Layer Depth Parameterization and Ocean Surface Cooling Induced by Tropical Cyclones. *Ocean Modelling*, 195, 102514. <http://doi.org/10.1016/j.ocemod.2025.102514>
13. Edson, J.B., Jampana, V., Weller, R.A., Bigorre, S.P., Plueddemann, A.J., Fairall, C.W., Miller, S.D., Mahrt, L., Vickers, D. [et al.], 2013. On the Exchange of Momentum over the Open Ocean. *Journal of Physical Oceanography*, 43(8), pp. 1589-1610. <http://doi.org/10.1175/JPO-D-12-0173.1>
14. Soloviev, A.V., Lukas, R., Donelan, M.A., Haus, B.K. and Ginis, I., 2014. The Air-Sea Interface and Surface Stress under Tropical Cyclones. *Scientific Reports*, 4(1), 5306. <http://doi.org/10.1038/srep05306>
15. Longuet-Higgins, M.S., 1965. The Response of a Stratified Ocean to Stationary or Moving Wind-Systems. *Deep Sea Research and Oceanographic Abstracts*, 12(6), pp. 923-973. [http://doi.org/10.1016/0011-7471\(65\)90814-4](http://doi.org/10.1016/0011-7471(65)90814-4)
16. Donelan, M.A., Haus, B.K., Reul, N., Plant, W.J., Stiassnie, M., Graber, H.C., Brown, O.B. and Saltzman, E.S., 2004. On the Limiting Aerodynamic Roughness of the Ocean in Very Strong Winds. *Geophysical Research Letters*, 31(18), 19460. <http://doi.org/10.1029/2004gl019460>
17. Takagaki, N., Komori, S., Suzuki, N., Iwano, K., Kuramoto, T., Shimada, S., Kurose, R. and Takahashi, K., 2012. Strong Correlation between the Drag Coefficient and the Shape of the Wind Sea Spectrum over a Broad Range of Wind Speeds. *Geophysical Research Letters*, 39(23), 53988. <http://doi.org/10.1029/2012GL053988>
18. Ye, L., Li, Y. and Gao, Z., 2022. Surface Layer Drag Coefficient at Different Radius Ranges in Tropical Cyclones. *Atmosphere*, 13(2), 280. <http://doi.org/10.3390/atmos13020280>
19. Ermakova, O., Rusakov, N., Poplavsky, E., Sergeev, D. and Troitskaya, Y., 2023. Friction Velocity and Aerodynamic Drag Coefficient Retrieval from Sentinel-1 IW Cross-Polarization C-SAR Images under Hurricane Conditions. *Remote Sensing*, 15(8), 1985. <http://doi.org/10.3390/rs15081985>

Submitted 20.12.2024; approved after review 08.02.2025;  
accepted for publication 13.03.2025.

*About the authors:*

**Pavel D. Pivaev**, Junior Researcher, Marine Hydrophysical Institute of RAS (2 Kapitanskaya Str., Sevastopol, 299011, Russian Federation), Engineer-researcher, Satellite Oceanography Laboratory, Russian State Hydrometeorological University (98 Malookhtinskiy Ave., Saint Petersburg, 195196, PHYSICAL OCEANOGRAPHY VOL. 32 ISS. 3 (2025) 425

Russian Federation), **SPIN-code: 4200-1129, ORCID ID: 0000-0003-2218-5774, ResearcherID: JBJ-6552-2023, Scopus Author ID: 57430050200**, pivaev.pavel@gmail.com

**Vladimir N. Kudryavtsev**, Head of the Satellite Oceanography Laboratory, Russian State Hydrometeorological University (98 Malookhtinskiy Ave., Saint Petersburg, 195196, Russian Federation), Leading Researcher, Marine Hydrophysical Institute of RAS (2 Kapitanskaya Str., Sevastopol, 299011, Russian Federation), DSc. (Phys.-Math.), **SPIN-code: 2717-5436, ORCID ID: 0000-0002-8545-1761, ResearcherID: G-1502-2014, Scopus Author ID: 7102703183**, kudr@rshu.ru

*Contribution of the co-authors:*

**Pavel D. Pivaev** – writing of the original draft of the manuscript, data curation, visualization and processing, discussion of the results

**Vladimir N. Kudryavtsev** – conceptualization, review and editing of the manuscript, discussion of the results

*The authors have read and approved the final manuscript.*

*The authors declare that they have no conflict of interest.*